VILNIUS TECH
Vilnius Gediminas Technical University

AVIATION

ANALYTICAL CALCULATION APPROACH FOR ROCKET NOSE CONE STRUCTURE WITH ORTHOTROPIC MATERIAL

Arief Budi SANJAYA✉, Haryadi ABRIZAL, Muhammad Dito SAPUTRA, Rahmat Alfi DUHRI, Muhamad Hananuputra SETIANTO, Ahmedi ASRAF, Hendra GANTINA

Research Center for Rocket Technology, National Research and Innovation Agency, Bogor, Indonesia

Abstract. The Authors of this research developed an analytical calculation method to estimate the strength of nose cone structures made of orthotropic materials, which were crucial components in aircraft and spacecraft. Strength analysis of nose cones had been comprehensively addressed for isotropic materials; however, the lack of efficient approaches for orthotropic materials presented a challenge. In this research, a new analytical method was proposed, combining membrane stress theory for isotropic materials with classical laminate theory for orthotropic materials. This approach enabled the determination of stresses on the nose cone shell structure in both meridional and circumferential directions in an efficient and straightforward manner. The analysis results indicated that the developed analytical method exhibited stress distribution trends similar to those obtained using the Finite Element Method. Stresses in the +45° and –45° direction, as well as in-plane shear stress and Tsai-Wu failure indices, showed trend similarity between the two methods. Despite specific numerical differences in the calculation results, these consistent trends suggested that the analytical method could serve as a tool for the preliminary design of a nose cone structure with a similar configuration analyzed in this study.

1. Introduction

A nose cone is a shell structure with a doubly curved surface rotated about its axis, i.e., shells of revolution. Positioned at the foremost part of flight vehicles, the nose cone is subjected to various flight loads, including aerodynamic and thermal loads, as well as gravitational forces. The drag, which becomes main aerodynamic load in nose cone, consist of three types, i.e. skin friction drag, pressure drag, and wave drag (Mathew et al., 2021). Hence, the nose cone design has been driven by requirement of aerodynamic drag minimization, from which some shapes are designed such as conical, ogive, and Power series. Some of these nose cone shapes are regarded as optimal designs depending on the mach region and the resulting heating characteristics (Ukirde & Rathod, 2023). In some cases, nose cones contain antenna for signal transmission of their payload, therefore radio-transparent properties must also be considered (Purwoko et al., 2023).

CFD is a numerical method commonly used to study aerodynamic phenomena in aerospace engineering. It is used to solve the Navier-Stokes equation, which is derived from three fundamental laws, i.e., continuity, momentum, and energy conservation law, governing the fluid behavior passing a rigid body (Zawawi et al., 2018). Several works

in CFD simulation are presented. Iranmanesh et al. (2023) and Shi et al. (2023) performed a CFD simulation to investigate coolant jet flow in a nose cone, each with different geometry and configuration, during hypersonic flight. They successfully identified the optimum jet position to provide adequate protection from aerodynamic heating for the nose cone. In structural applications, CFD is utilized to calculate the flight load of aircraft and launch vehicles. Kuitche and Botez (2017) performed a CFD simulation along with the Vortex Lattice Method and DATCOM procedure to obtain various aerodynamic coefficients, including the drag coefficient, as a function of the angle of attack and angle of sideslip. The drag coefficient is a quantity to express the quasi-steady drag force nondimensionally (Loth et al., 2021).

In aerospace engineering, laminated composite material has been extensively used due to its superior mechanical characteristics, e.g., lightweight, high strength and stiffness, and corrosion resistance, compared to traditional materials such as metals and alloys (George et al., 2021). For example, the laminated composite material can be found in helicopter rotor blades (Ahmad et al., 2020), aircraft fuselage (Aribowo et al., 2023), and nose cones of the launch vehicles (Kurdianto et al., 2023). Laminated composite can also be combined with foam, such as

extruded polystyrene, to form a sandwich structure and be used in UAV-fixed wings (Karpenko et al., 2023). In more advanced applications, a multifunctional wing that allows active actuation and energy harvesting to be performed simultaneously has been developed using laminated composite material (Tsushima & Su, 2017). In simple structures such as cylindrical tubes, the composite material has been utilized in hydraulic actuators. A thorough review of the development of composite hydraulic actuators, including manufacturing, testing, and modeling, is carried out by Lubecki et al. (2022). Various actuator designs have been employed, such as steel liners and nanocomposite coating, which are manufactured by filament winding. Analytical modeling was included in calculating the stress distribution given the axial force, internal pressure, and temperature. Besides hydraulic actuators, composite cylinder tubes are widely incorporated in rocket motor casing design, as can be found in research works by Srivastava et al. (2022a, 2022b) and Davies et al. (2022).

Discussions on methods to predict the mechanical behavior of composite materials have been extensively covered in previous studies. Tita et al. (2011) delved into a theoretical framework aiming to estimate the mechanical behavior of thick composites by outlining analytical formulations and influential parameters. For relatively simple structures, the CLT approach combined with numerical analysis such as FEM can yield predictions of composite material characteristics with reasonable results. Gheshlaghi et al. (2006) analyzed composite cylindrical shells using CLT combined with shell elasticity equation theory. It was concluded that CLT and FEA can produce consistent results for simple models like cylindrical tubes. In addition to shell theory, the development of analytical equations for calculating stress and deformation in composite tube laminates was pioneered by Logan and Widera (1989). The authors developed equations to calculate the structure of nonhomogeneous anisotropic shells of revolution through the Hellinger-Reissner variational principle and asymptotic expansion technique.

Strength analysis of isotropic nose cone structures has been thoroughly discussed in several engineering textbooks under the doubly-curved shell of the rotation section (Reddy, 2007; Ugural, 2017; Ventsel & Krauthammer, 2001). The equations are relatively straightforward and can be implemented with minimum effort. Meanwhile, analytical solutions for determining the strength of doubly-curved composite structures can be less efficient and pose a greater challenge due to the complex formula derivations. Sayyad and Gugal (2019) proposed an analytical formulation to evaluate static bending and free vibration response of spherical orthotropic shells using the Higher-order Shear Deformation Theory. However, the formulation only works with simply supported boundary conditions. For the general case, Aghdam et al. (2011) developed an analytical formulation for static bending of the thick functionally-graded orthotropic conical shell using the first-order shear deformation theory combined with

the extended Kantorovich numerical method. Further exploring shell behavior, Guo et al. (2021) conducted a free vibration analysis of composite conical shells employing the Walsh series method. Based on the first-order shear deformation theory, their model transforms complex multivariable differential equations into simpler linear algebraic equations, enhancing solvability and accuracy. Similarly, Shadmehri et al. (2012) used a semi-analytical approach to study the buckling of conical composite shells under axial compression. Employing first-order shear deformation shell theory and linear strain-displacement relationships, they resolved the equations using the Ritz method and concluded that critical buckling loads decrease with increasing semi-cone angles, especially beyond 20 degrees, and with increased fiber orientation in angle-ply shells.

In order to address this issue, this study proposed a simpler and more efficient analytical calculation method for nose cones made of orthotropic materials. This method integrates membrane stress theory for isotropic materials with CLT for orthotropic materials. The membrane stress theory is used to determine the stress resultants in the shell structure in both the meridional and parallel directions. Subsequently, based on the obtained stress resultants values, the stresses occurring in the laminates in both directions of the shell structure are evaluated using CLT. The analytical procedure is validated using FEM afterward with a more realistic model, incorporating glued contact and bolt holes. The approach taken is expected to contribute to the development of more efficient analytical methods for shells of revolution structures, particularly nose cones.

2. Analytical method

2.1. Stress resultant on a thin shell

In the thin elastic shell, the bending and twisting moments can be neglected, provided that suitable boundary and loading conditions are given. This implies that the forces on the thin shells only act within the surface plane, i.e., in-plane loading. Due to this, the thin elastic shell falls into a membrane state, allowing only membrane stress to act on the structure, hence the name *membrane stress theory*. However, the theory is not valid for structural components with geometric discontinuities, such as changes in radius or thickness and sharp inclinations. The bending stress theory of thin shells is utilized instead in such structures. Nevertheless, the membrane stress theory is considered adequate for analyzing stress in most thin shell structures.

A nose cone is a doubly-curved shell of revolution structure defined by the midsurface geometrical parameters, e.g. r_1, r_2, and ϕ. As the shell of revolution is subjected to an axisymmetric external pressure load, membrane stress resultants N_ϕ and N_θ are generated as shown in Figure 1. The membrane stress resultant is another term for force per unit length of meridian or parallel curve. The relationship between the two stress resultants and the
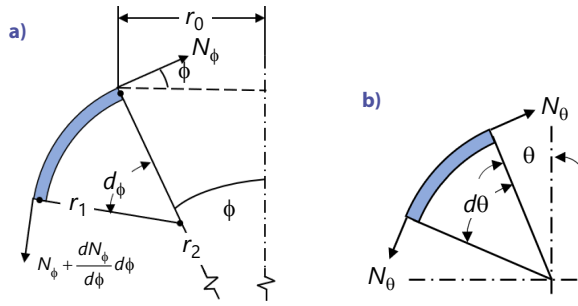
a)

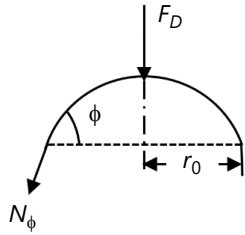**Figure 1.** Force analysis on shell of revolution structure: a – front view; b – top view

Figure 2. Ilustration of forces on nose cone

external pressure load is described as follows (Zingoni & Enoma, 2020):

$$\frac{N_\phi}{r_1} + \frac{N_\theta}{r_2} = -p_z. \tag{1}$$

Meanwhile, the stress resultant N_ϕ is evaluated using Equation (2).

$$N_\phi = \frac{-F_D}{2\pi r_0 \sin\phi}. \tag{2}$$

The force F_D, as shown in Figure 2 represents the external pressure p_z acting on the nose cone surface. In this study, F_D is equivalent to the aerodynamic drag force generated by the static pressure. Hence, by knowing the value of N_ϕ, the stress resultant N_θ is calculated using Equation (1).

2.2. Classical laminate theory (CLT)

The CLT is commonly used to analyze stress in fiber composite laminates. This theory assumes that the thickness of the laminate is much smaller than its other dimensions, hence Kirchoff's hypothesis applies. The hypothesis states that the cross-section of a laminate remains perpendicular to the laminate midplane when subjected to bending loads. This implies that transverse shear strains are neglected, and thus transverse shear stresses are not taken into account in the calculation.

Laminate analysis using CLT begins with evaluating the midplane strains and global curvature. The relationship between the force per unit length $N = \{N_x, N_y, N_{xy}\}^t$

and moments per unit length $M = \{M_x, M_y, M_{xy}\}^t$ to the

strains in the midplane $\varepsilon_0 = \{\varepsilon_{x0}, \varepsilon_{y0}, \varepsilon_{xy0}\}^t$ and curvatures in global coordinates $\kappa = \{\kappa_x, \kappa_y, \kappa_{xy}\}^t$ is expressed in Equation (3) (Casavola et al., 2016):

$$\begin{Bmatrix} N \\ M \end{Bmatrix} = \begin{bmatrix} A & B \\ B & D \end{bmatrix} \begin{Bmatrix} \varepsilon_0 \\ \kappa \end{Bmatrix}, \tag{3}$$

where matrix $\begin{bmatrix} A \end{bmatrix}$, $\begin{bmatrix} B \end{bmatrix}$, and $\begin{bmatrix} D \end{bmatrix}$ is expressed as follows:

$$\begin{bmatrix} A, B, D \end{bmatrix} = \sum_{i=1}^{n} Q_i \left[(z_i - z_{i-1}), \right.$$
$$\left. \frac{1}{2}(z_i^2 - z_{i-1}^2), \frac{1}{3}(z_i^3 - z_{i-1}^3) \right]. \tag{4}$$

Subscript i indicates i-th layer starting from the neutral axes of the laminate. Then, by using $\{\varepsilon_0\}$ and $\{\kappa\}$ obtained from Equation (3), the laminate strains at each z-position in global coordinates is determined using Equation (5).

$$\{\varepsilon\} = \{\varepsilon_0\} + z\{\kappa\}. \tag{5}$$

The global strains are then transformed into local coordinates using Equation (6), which are then used as the basis for calculating the local stresses of each lamina in Equation (7). Each lamina's strain and stress values are subsequently used to determine failure indices.

$$\{\varepsilon_l\} = [T]^t \{\varepsilon\}; \tag{6}$$

$$\{\sigma_l\} = [Q_l]\{\varepsilon_l\}. \tag{7}$$

2.3. Nose cone geometry

The nose cone design is based on the Power series shape, which is described using Equation (8) (Crowell, 1996):

$$y = R\left(\frac{x}{L}\right)^n, \tag{8}$$

for $0 \le n \le 1$. All variables in Equation (8) are shown in Figure 3 with $y = r_0$ in case of shell of revolution structure. Meanwhile, $n = 3/4$ is used in this study, representing the Three-Quarter Power series type.

In calculation, it is convenient to express the Equation (8) as a function of y, i.e. f(y), hence a manipulation is needed to match the equation with Figure 3. This manipulation leads to Equation (9).

$$x = L\left(\frac{r_0}{R}\right)^{4/3}. \tag{9}$$

The second derivatives of x with respect to r_0 from Equation (9) are then computed to obtain the radius r_1.
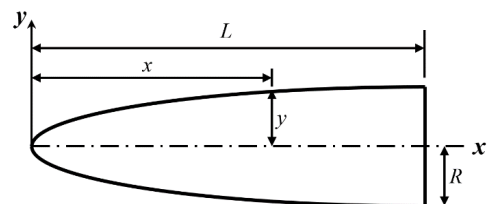

Figure 3. Nose cone geometry

2.4. Discretization and calculation procedure

The analytical calculation is performed by discretizing the nose cone into several small segments. This method ensures minimum calculation error under sufficiently small segments, resulting in comparable results to those obtained through CAE software. The precision of this method is critical for validating design parameters and ensuring the structural integrity of the nose cone under various loading conditions.

By knowing the pressure distribution on the nose cone's outer surface, the aerodynamic drag force can be estimated analytically by discretization. The pressure distribution is obtained through CFD analysis as outlined in Section 3.4. The resultant force F_n, as shown in Figure 4a, is the product of static pressure at k-th segment and the corresponding segment's surface area. The resultant force F_n is decomposed into two force components, i.e., $F_n\sin\varphi_n$ and $F_n\cos\varphi_n$ as illustrated in Figure 4b. Drag force at k-th segment, $F_{D,k}$, is then defined by Equation (10):

$$F_{D,k} = \sum_{n=1}^{k} F_n \cos\varphi_n. \tag{10}$$

The obtained $F_{D,k}$ value is then substituted into Equation (2) to obtain $N_{\phi,k}$ which is then used to calculate $N_{\theta,k}$ in Equation (1). These two stress resultant evaluated for each k-th segment is substituted into Equation (3), i.e. $N_x = N_{\phi,k}$ and $N_y = N_{\theta,k}$. The stress is subsequently computed through the procedure described in Section 2.2. The results of stress calculations are then evaluated using the Tsai-Wu laminate failure criteria found in literature, e.g. a research work by Kolios and Proia (2012).
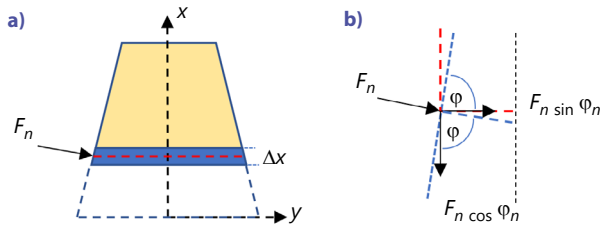

Figure 4. Force analysis on nose cone structure: a – force loading on segments; b – decomposition of force F_n

3. Finite element method (FEM)

3.1. Overview

In order to determine the reliability and accuracy of the calculation method applied in this study, an evaluation is carried out by comparing the analytical calculation with FEM results. The software used for FEM analysis is MSC Patran as a pre-processor and MSC Laminate Modeler for composite laminate modeling. Laminate Modeler provides advantages in modeling the draping process during manufacturing stages, allowing fibre direction distortions to be considered in stress analysis, thus improving the accuracy of the analysis results. Furthermore, the MSC Nastran SOL 101, which is a linear static analysis solver, is used to

handle the analysis assuming the absence of geometry, material, and contact nonlinearities.

3.2. Mathematical formulation

The formulation of Finite Element Method for 3D element model is expressed by Equation (11):

$$\int_{V_e} [B_m]^t [C][B_m] dV \{U\} =$$

$$\int_{V_e} [N]^t \{X\} dV + \int_{S_e} [N]^t \{T\} dS, \tag{11}$$

while for multilayered 2D shell element in composite modeling is defined by Equation (12):

$$\oint_{A_e} \left([B_0]^t [A][B_0] + 2[B_0]^t [B][B_l] + \right.$$

$$\left. [B_l]^t [D][B_l] dA \{U\} \right) =$$

$$\oint_{S_l} \left([N] \left(T_n + \frac{\partial M_{ns}}{\partial s} \right) - \right.$$

$$\left. [B] \binom{\cos\varphi}{\sin\varphi} M_n \right) ds +$$

$$\oint_{A_e} [N] q dA. \tag{12}$$

Equation (11) and (12) can be rewritten in a Hooke's Law form as follows:

$$[K]\{U\} = \{F\}. \tag{13}$$

Equation (11) and (12) are solved by performing Gaussian quadrature integration to obtain the stiffness matrix and nodal force vector. Once these two quantities are acquired, the displacement is computed through stiffness matrix inversion in Equation (13).

In general, the stress in Finite Element Method is evaluated by employing the following constitutive relation

$$\{\sigma\} = [C]\{\varepsilon\}. \tag{14}$$

In term of nodal displacement, nodal strain is expressed by Equation (15)

$$\{\varepsilon\} = [B_m]\{U\}. \tag{15}$$

The nodal stress both in 3D element FEM and 2D shell element model is obtained by substituting Equation (15) to Equation (14), leading to Equation (16) as follows:

$$\{\sigma\} = [C][B_m]\{U\}, \tag{16}$$

where $[B_m]$ for 2D shell element model is defined by Equation (17):

$$[B_m] = [B_0] + z[B_l]. \tag{17}$$

3.3. Geometrical modeling and meshing

The nose cone assembly consists of two main components: the nose cone tip and the nose cone body, both of which are made of steel and S-glass/epoxy composite,
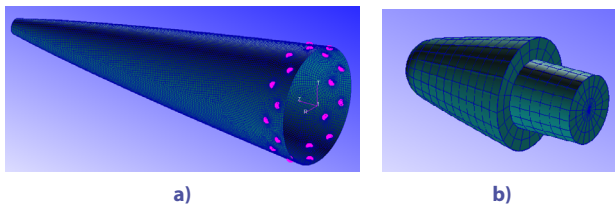
Figure 5. FEM model: a – the nose cone body; b – the nose cone tip

respectively. In the modeling process, the nose cone body is modeled in 2D surface format as required by Laminate Modeler. This 2D modeling approach allows for accurate simulation of layered composite structure while reducing the computational time and cost. Meanwhile, the nose cone tip is represented in 3D solid body to capture the geometrical complexity of the component. This comprehensive modeling approach ensures that both components are accurately represented without introducing unnecessary complication to the entire model.

The nose cone body is represented in the FEM model using hybrid 2D elements, which incorporate both Quad and Tria elements with a GEL of 8 mm as shown in Figure 5a. Meanwhile, the nose cone tip is modeled using 3D elements as illustrated in Figure 5b. Due to the sufficiently small GEL, both 2D and 3D element used are linear element type.

3.4. Load and boundary condition

The external force acting on the nose cone during flight results from the surrounding static air pressure during flight. A CFD analysis was performed on the nose cone to determine this pressure distribution accurately. The analysis provides a detailed map of the static air pressure acting on the entire surface of the nose cone, as shown in Figure 6. The load assumes that the pressure varies only along the longitudinal axis, with maximum pressure of 612.8 kPa occurs at the nose cone tip area. This pressure distribution will be used as the loading in the FEM as well as the analytical analysis, applied to the entire outer surface of the nose cone including the tip and body. This load application allows the assessment of the nose cone structural response under realistic flight conditions.
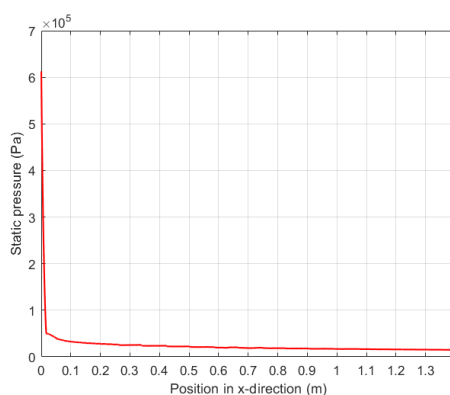

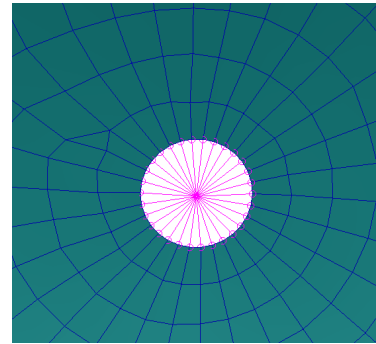**Figure 6.** Load from static air pressure

Figure 7. MPC in the form of RBE2

The nose cone body includes bolt holes as a means of structural connection to other structural components. Bolt connection modeling is done by applying boundary conditions to the bolt holes using MPC in the form of RBE2. Dependent nodes are applied to nodes around the holes, while independent nodes are applied to nodes in the middle of the bolt holes, as shown by magenta coloured entities in Figure 7. The complete RBE2 modeling for all holes is shown in Figure 5a. Boundary conditions that restrict displacement are applied to independent nodes by locking nodal movement in the translational direction (UX = UY = UZ = 0). Applying this MPC creates stress concentrations that are more realistic than those in fully fixed constraint boundary conditions.

3.5. Contact modeling

Adhesive contact between nose cone components is modeled by assuming the nose cone tip and body as the master and slave surface, respectively. The nose cone body, primarily those close to the tip, cannot be modeled with the same precision as in the 3D CAD model, resulting in an overlap of approximately 7.3 mm, as illustrated in Figure 8. A tolerance setting of about 8 mm addresses this issue and ensures adequate contact between the two components, with approximately 95% of elements of both components touching each other.

Figure 8. Overlap between the body and tip of the nose cone

3.6. Draping simulation

Laminate Modeler has the capability of modeling composite materials in the form of UD fiber and weave. The nose cone composite material consists of woven fiber oriented at +45/–45° with respect to the longitudinal axis. The arrangement of the weave composite is created using the Scissor Drape method. In the Laminate Modeler, a successful draping simulation is followed by the generation of flat patterns of composite fabric, as shown in Figure 9.
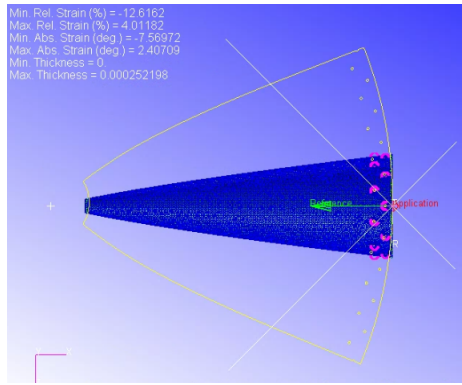
Figure 9. Single ply flat pattern of nose cone composite

The figure shows a slight distortion in the fiber orientation angle, indicated by the minimum and maximum strains of −7.57° and 2.41°, respectively.

Assuming a female mold is used, the arrangement of 92 laminates starts from the mold's interior surface towards the midpoint of the parallel circle. Therefore, the first laminate represents the outer radius of the nose cone while the last laminate, i.e. the 92nd layer, represents the inner radius of the nose cone.

3.7. Mechanical properties

Common mechanical characteristics of steel are used in this analysis with an E of 200 GPa, ρ of 7700 kg/m^3, and ν of 0.3. Meanwhile, the nose cone body made of S-glass/epoxy composite has a +45/–45 woven ply thickness of 0.25 mm with a total of 92 plies. The mechanical characteristics of S-glass/epoxy composite are taken from the literature with E_1 and E_2 of 28 GPa each, $\nu_{12} = \nu_{21}$ of 0.15, G_{12} of 12 GPa, G_{13} and G_{23} of 6 GPa each, and maximum tensile stress σ_{1t}, σ_{1c}, σ_{2t}, σ_{2c}, and maximum shear stress τ_{12} each of 480 MPa, 440 MPa, 480 MPa, 440 MPa, and 320 MPa (Guan et al., 2014).

3.8. Solver

In this study, linear static solver is utilised to compute stress and deformation of the nose cone FEM model. Linear static solver computes the effect of static loading conditions on a structure, ignoring the damping and inertia effect caused by the time dependent load. The static loading assumptions are valid for most structural design problem, including the nose cone. Therefore, linear static solver is deemed sufficient to solve the FEM model of nose cone.

In Finite Element Method, the analysis involves solving large linear system of Equation (13), which requires matrix decomposition to minimize the computational time. Subsequently, forward-backward substitution is applied to obtain the direct solution of linear system. MSC Nastran employs sparse algorithm to execute the calculation of forward-backward substitution, which is essential to gain efficient computational process.

4. Result and discussion

4.1. FEM analysis

FEM displacement and stress results were thoroughly investigated to ensure their validity as a benchmark against the analytical method. Overall, FEM results are deemed sensible and consistent with the expected theoretical outcomes. Therefore, the FEM results remain reliable and can be confidently used as a baseline for comparison with the analytical method.

The nose cone deformation is depicted in Figure 10a and 10b. The red net in the Figure represents the undeformed configuration of the nose cone assembly. The deformation has been upscaled 20 times to obtain better visualization since the maximum deformation is minuscule, measuring only 0.00386 mm. As expected, axisymmetric deformation is observed in the nose cone body due to the applied load varying only along the longitudinal axis. Additionally, the maximum deformation occurs at the nose cone tip, which is reasonable due to the largest static pressure arising in the same area.

Meanwhile, the axisymmetric stress results in the nose cone body, as shown in Figure 11a, 11b, and 11c, are also reasonable since the deformation is directly proportional to the stress. To maintain the report's conciseness, the figures only display stresses for the 1st layer. Additionally, as expected, the compressive stress for local 1- and 2-direction increases as the x-position increases, indicated by smooth element colour transition toward darker shade. This increase in stress is attributed to the rising stress resultant along the longitudinal axis. Upon reaching the bolt hole section, the stress becomes concentrated at a single point, leading to stress relief in the surrounding area. Meanwhile, in-plane shear stress tends to remain constant in the nose cone body. However, some regions show a transition from tensile to compressive stress due to the split line formation during the drape simulation. Lastly, similar to the local 1- and 2-direction, the stress concentration occurs at a point on the bolt hole and relieves in-plane shear stress in its vicinity.
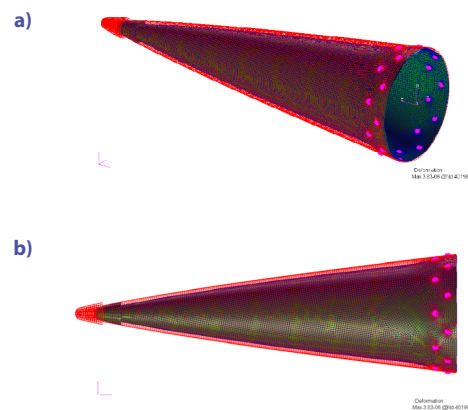

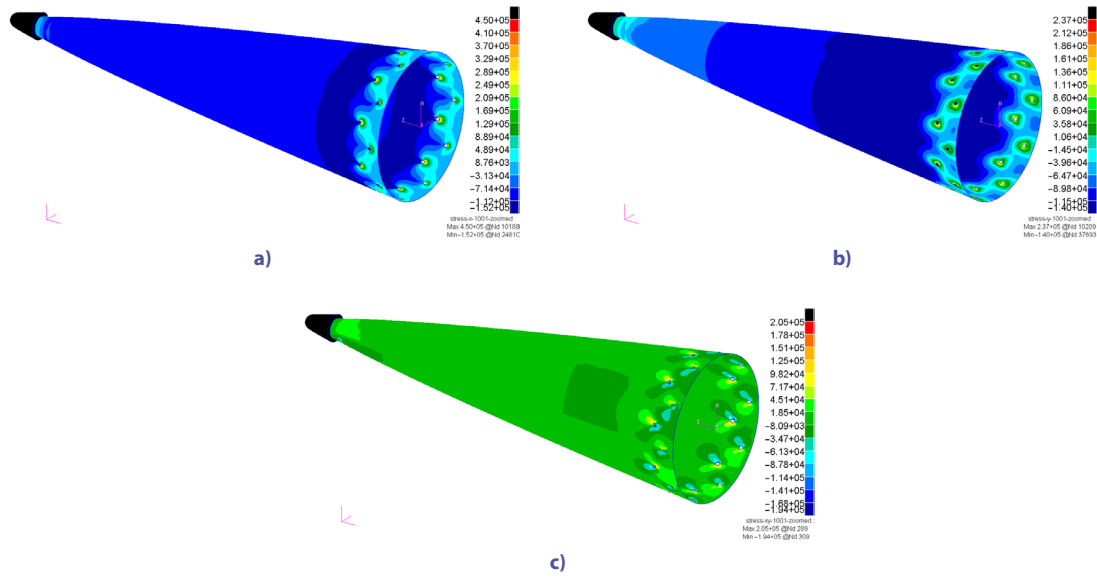**Figure 10.** FEM deformation results: a – isometric view; b – front view

Figure 11. FEM stress results for the 1st layer: a – local axis 1-direction; b – local axis 2-direction; c – in-plane shear

4.2. Analytical approach analysis

The stress resultants are a matter of concern as they determine the accuracy of analytical computation of the stress distribution in the nose cone. The analytical calculations show that the compressive stress resultant in the parallel direction is higher than that in the meridian direction at all observation points, as seen in Figure 12. However, since the stress resultant is force per unit length of the meridional and parallel curve, the force in both directions is similar owing to the geometry of the nose cone, wherein the cross-sectional area expands towards the base. This results in similar stress distribution along the x-axis for +45° and –45° fiber directions, as shown in Figure 13a and Figure 13b. Additionally, both compressive stress resultants in the meridional and parallel directions escalate due to increased drag force along the x-axis. Due to its aerodynamic shape, the drag force
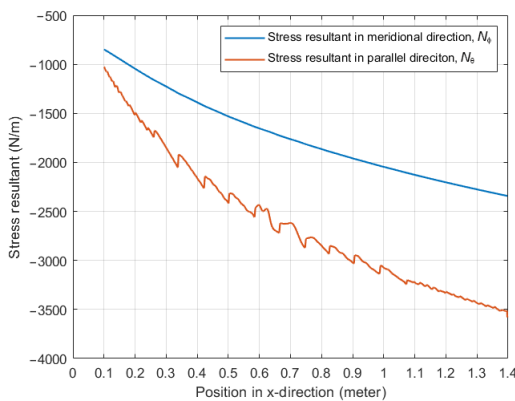
is small at the fore section and reaches a maximum at the aft section of the nose cone. Therefore, based on this observation, the stress resultant results are considered reasonable.

The stress and Tsai-Wu failure indices observation for both analytical and FEM methods are performed along the central axis. The comparison of two results is shown in Figure 13a, Figure 13b, Figure 13c, and Figure 13d, in which the FEM results are presented for three different layers, i.e., the 1st, 46th, and 92nd layers, while analytical calculations are only performed in the middle layer. Overall, the analytical method depicts satisfactory consistency in the resulting trend, primarily in stress-concentration-free areas, i.e., between two vertical dotted lines in the figures. In areas near the nose cone tip and base, i.e., areas beyond the first and second vertical line, significant deviation between analytical and FEM is apparent due to stress concentration. Adhesive contacts and bolt holes are the primary sources of stress concentration, which are not included in the analytical modeling. After exiting the bonded joint area, the stress concentration does not relieve, which explains the substantial discrepancy between analytical and FEM results for three stresses up to approximately 0.65 meters. Meanwhile, shear stress in analytical shows notable deviation with FEM, both in magnitude and sign value, along the x-axis. The FEM curve starts from a negative shear value and decreases towards zero as it approaches approximately 0.48 meters, and eventually, the positive shear starts to build up. However, this does not pose an issue since the sign of the shear stress is irrelevant when calculating the Tsai-Wu failure indices. Additionally, the Tsai-Wu failure indices are not sensitive to shear stress, as shown by the Tsai-Wu relative error in Figure 14, therefore the shear stress magnitude deviation has little impact on the Tsai-Wu indices.
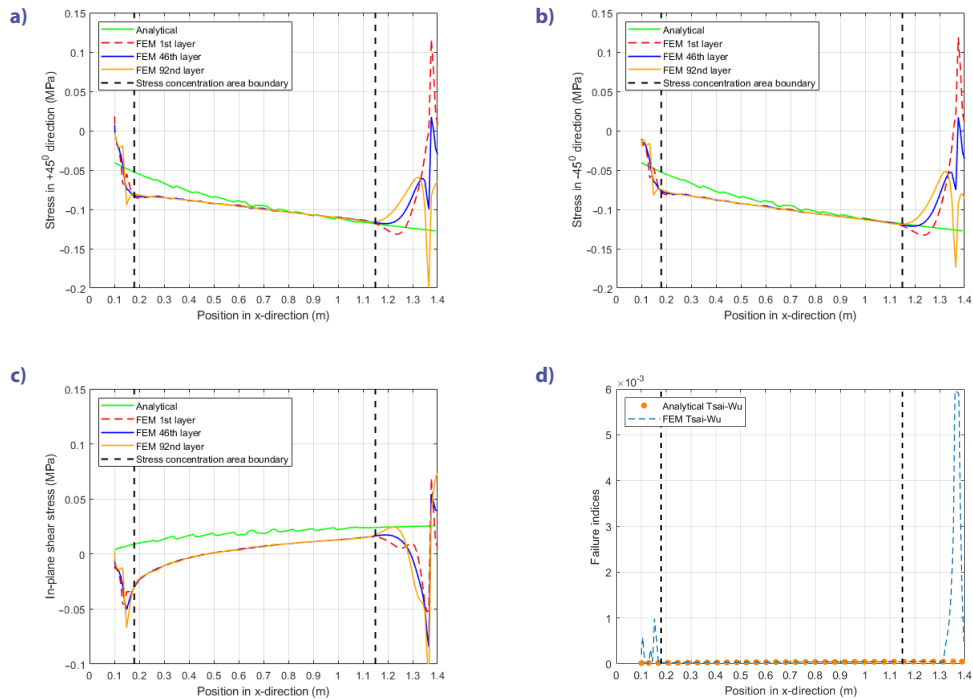

Figure 12. Stress resultants in the meridional and parallel directions obtained from the analytical calculation

Figure 13. Distribution along the longitudinal axis: a – stress in +45°; b – stress in –45°; c – in-plane shear stress; d – Tsai-Wu failure indices

4.3. Relative error analysis

The relative error distribution of the analytical method with respect to FEM result in +45°, –45°, and shear as well as Tsai-Wu failure indices is presented only for the stress-concentration-free area in Figure 14. The figure reveals that the relative error for all stresses and Tsai-Wu indices are significant at the fore section, after which the relative error gradually reduces as the position progresses in the x-direction. As expected, the relative error of stresses in the +45° and –45° direction are closely aligned, which is consistent with the similarity in their magnitude trends depicted in Figure 13a and Figure 13b. Meanwhile, the relative error for shear stress diverges considerably from the other two stresses without reaching zero value. However, shear stress contribution to Tsai-Wu failure indices is minuscule, resulting in the Tsai-Wu relative error virtually resembling that of the +45° and –45° curves.
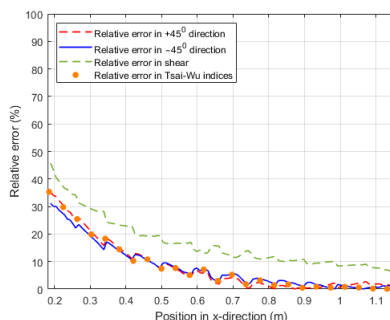
The maximum relative error for Tsai-Wu failure indices in the zone unaffected by stress concentration is notable, i.e., approximately 35%. However, considering the trend similarities in stresses and failure indices, the analytical method is deemed an adequate tool to evaluate the composite nose cone integrity in the section with slight stress concentration. For preliminary design purposes of similar nose cone configuration with varying thickness and fiber composite layup, the proposed method provides a good approximation of stress distribution before proceeding into the FEM modeling to obtain more precise stress data.

4.4. Fibre distortion compensation analysis

A trial was conducted to investigate the effect of fibre distortion compensation in the analytical model. Woven layups of ±48.8° and ±43.8° are introduced in the analytical method to simulate FEM models' maximum and minimum fibre distortion of −7.57° and 2.41°, respectively. The new layups are applied homogeneously to all nose cone body sections. The relative errors of stresses and Tsai-Wu failure indices produced by both new layups are subsequently compared with the relative error of the original ±45° layup.

The deviation of relative error is observed in the local 1- and 2-direction results. The relative error of stress in the local 1-direction of three layups, i.e. +45°, +48.8°, and +43.8° direction, is depicted in Figure 15a. In the figure, the relative error of stress in the +43.8° direction shows an almost negligible deviation from the +45° direction for all x-positions in the nose cone body. On the contrary, +48.8° layup exhibits significant relative error improvement between the onset of a stress-concentration-free area and a location

Figure 14. Relative error distribution along the longitudinal axis

approximately 0.8 meters away before showing a decline. Meanwhile, Figure 15b shows the relative error of stress in the local 2-direction of the identical three layups, i.e., 45°, –48.8°, and –43.8° direction. Similar to the finding in Figure 15a, the relative error of the –43.8° direction is also closely matched with the –45° direction. However, the relative error of –48.8° direction behaves oppositely to that of +48.8°, worsening along the nose cone's longitudinal axis. These findings suggest that larger distortions will have a greater impact on the relative error in the stress of local 1- and 2-direction, either improving or worsening it.

Unlike local 1- and 2-directions, the deviation trend is not seen in the relative error of in-plane shear and Tsai-Wu failure indices. Figure 15c illustrates the comparison of relative error of in-plane shear for all three layups, showing that ±48.8° and ±43.8° layup deviates slightly from the ±45° layup. This finding suggests that the fibre distortion of –7.57° and 2.41° are insignificant enough to affect the shear stress generation in the layup. Similarly, Figure 15d shows that the ±48.8° and ±43.8° layups have a negligible deviation of Tsai-Wu failure indices with ±45° layup. The significant deviation in local 1- and 2-direction of ±48.8° layup does not impact the relative error of Tsai-Wu failure indices, attributed to the nonlinear relationship between stresses and failure indices.

In conclusion, the introduction of fibre distortion of –7.57° and 2.41° in the analytical method does not provide any meaningful improvement to the relative error of each stress and Tsai-Wu failure indices. This finding indicates that the variations in fibre orientation within this range do not substantially affect the accuracy or reliability of the method. Therefore, for the future application of this analytical method, user need not be concerned about potential fiber distortion to some extent. The method remains valid for use with designed fiber direction, allowing fast design process of the nose cone structure.

4.5. Remarks on fiber distortion

Fiber distortion is a common issue in the manufacturing of doubly-curved composite structures. As the layup is draped onto a curved surface, the fiber in woven material is subjected to in-plane shear. Hence, the material deforms and fiber distortion occurs due to intra-ply shear. The stress estimation, particularly using the analytical method, becomes unreliable in case of large fiber distortion. In this study, the analytical approach generates results comparable to those of the FEM model due to the insignificant fiber distortion effect in the FEM model. Care must be taken when dealing with fiber distortion exceeding 15 degrees since the analytical model might not be valid in such circumstances.

5. Conclusions

The analytical method for estimating the strength of nose cone structures with orthotropic materials has been successfully formulated based on membrane stress theory in thin shells and CLT. Membrane stress theory for a shell of revolution structures calculates stress resultants in meridional and parallel, which acts as inputs to CLT for evaluating the stress and Tsai-Wu failure indices. Nose cone geometry, which is based on a Power series shape, is discretized into small segments to compute the drag load
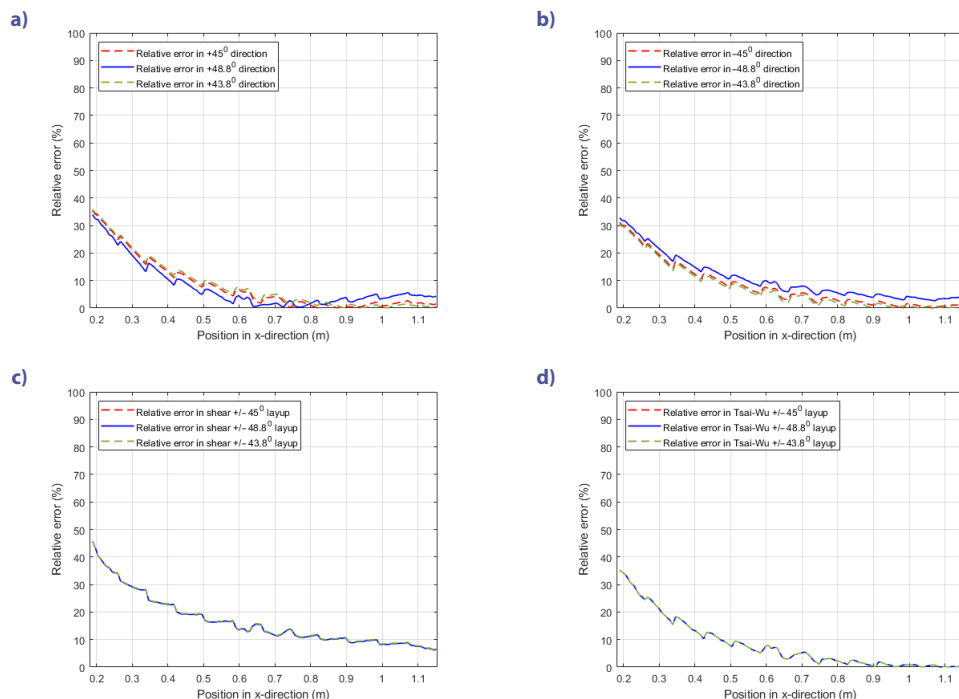

Figure 15. Relative error distribution for ±45°, ±48.8° and ±43.8° layup: a – stress in local 1-direction; b – stress in local 2-direction; c – in-plane shear stress; d – Tsai-Wu failure indices

analytically from static air pressure data obtained from CFD. The FEM model of nose cone structure, which consists of the nose cone tip and body, has been developed to validate the analytical formulation. The nose cone tip is constructed from steel material, while the nose cone body is fabricated from +45/–45 woven S-glass / epoxy composite. The model includes bonded joints and bolt holes on the fore and aft sections, respectively. The FEM model is solved using a linear static analysis solver by applying the static air pressure on the whole nose cone surface.

The FEM model provides reasonable results, allowing the model to be utilised as a benchmark against the analytical model result. Meanwhile, the analytical model findings indicate that the stress resultant results are sensible, both in meridional and parallel directions. The stresses and Tsai-Wu failure indices distribution generated by the analytical method exhibit similar trends to the values obtained through the FEM method with notable magnitude and relative error discrepancy in the area close to the bonded joint at the front section. Shear stress, compared to the other stresses, shows substantial relative error. However, it does not raise concern since shear stress has a limited influence on Tsai-Wu failure indices calculation. Even though inaccuracies are present to some extent, the trend similarities suggest that the analytical method developed can be used as a tool for the initial design of the nose cone structure with a similar configuration used in this research. The potential fibre distortion can be ignored to some degree when employing the analytical model since the introduction of fibre distortion insignificantly improved or worsen the relative error result. However, it is essential to proceed with caution in the presence of significant fiber distortion, as the analytical approach may no longer be applicable.

Acknowledgements

Author contribution

Arief Budi Sanjaya: conceptualization, methodology, analysis, writing – original draft. Haryadi Abrizal: conceptualization, methodology, writing. M. Dito Saputra: methodology, analysis, writing. Rahmat Alfi Duhri: methodology, writing. Muhamad Hananuputra Setianto: methodology, writing – editing & proofreading. Ahmedi Asraf: analysis, writing. Hendra Gantina: methodology, writing.

Disclosure statement

The authors declare that they have no known competing financial interest or personal/professional relationship from third parties that might be seen as affecting the work reported in this paper.

References

Ahmad, K., Baig, Y., Rahman, H., & Hasham, H. J. (2020). Progressive failure analysis of helicopter rotor blade under aeroelastic loading. *Aviation*, 24(1), 33–41. https://doi.org/10.3846/aviation.2020.12184

Aghdam, M. M., Shahmansouri, N., & Bigdeli, K. (2011). Bending analysis of moderately thick functionally graded conical panels. *Composite Structures*, 93(5), 1376–1384. https://doi.org/10.1016/j.compstruct.2010.10.020

Aribowo, A., Adhynugraha, M. I., Megawanto, F. C., Hidayat, A., Muttaqie, T., Wandono, F. A., Nurrohmad, A., Chairunnisa, Saraswati, Sh. O., Wiranto, I. B., Al Fikri, I. R., & Saputra, M. D. (2023). Finite element method on topology optimization applied to laminate composite of fuselage structure. *Curved and Layered Structures*, 10(1), 1–16. https://doi.org/10.1515/cls-2022-0191

Casavola, C., Cazzato, A., Moramarco, V., & Pappalettere, C. (2016). Orthotropic mechanical properties of fused deposition modelling parts described by classical laminate theory. *Materials & Design*, 90, 453–458. https://doi.org/10.1016/j.matdes.2015.11.009

Crowell, G. A. (1996). *The descriptive geometry of nose cones*. https://web.archive.org/web/20110411143013/http://www.if.sc.usp.br/~projetosulfos/artigos/NoseCone_EQN2.PDF

Davies, J., Grove, R., Bell, T., Rea, O., Furkert, M., Zhao, D., & Sellier, M. (2022). Preliminary design and test of high altitude two-stage rockets in New Zealand. *Aerospace Science and Technology*, 128, Article 107741. https://doi.org/10.1016/j.ast.2022.107741

George, J. S., Vasudevan, A., & Mohanavel, V. (2021). Vibration analysis of interply hybrid composite for an aircraft wing structure. *Materials Today: Proceedings*, 37, 2368–2374. https://doi.org/10.1016/j.matpr.2020.08.078

Gheshlaghi, R. M., Hojjati, M. H., & Daniali, H. R. M. (2006). Analysis of tubular composite cylindrical shells. In E. E. Gdoutos (Ed.), *Fracture of nano and engineering materials and structures* (pp. 333–334). Springer. https://doi.org/10.1007/1-4020-4972-2_164

Guan, Z. W., Aktas, A., Potluri, P., Cantwell, W. J., Langdon, G., & Nurick, G. N. (2014). The blast resistance of stitched sandwich panels. *International Journal of Impact Engineering*, 65, 137–145. https://doi.org/10.1016/j.ijimpeng.2013.12.001

Guo, S., Hu, P., & Li, S. (2021). Free vibration analysis of composite conical shells using Walsh series method. *Materials Research Express*, 8(7), Article 75303. https://doi.org/10.1088/2053-1591/ac0eb7

Iranmanesh, R., Alizadeh, A., Faraji, M., & Choubey, G. (2023). Numerical investigation of compressible flow around nose cone with Multi-row disk and multi coolant jets. *Scientific Reports*, 13(1), 787–787. https://doi.org/10.1038/s41598-023-28127-9

Karpenko, M., Stosiak, M., Deptuła, A., Urbanowicz, K., Nugaras, J., Królczyk, G., & Żak, K. (2023). Performance evaluation of extruded polystyrene foam for aerospace engineering applications using frequency analyses. *International Journal of Advanced Manufacturing Technology*, 126(11–12), 5515–5526. https://doi.org/10.1007/s00170-023-11503-0

Kolios, A. J., & Proia, S. (2012). Evaluation of the reliability performance of failure criteria for composite structures. *World Journal of Mechanics*, 2(3), 162–170. https://doi.org/10.4236/wjm.2012.23019

Kuitche, M., & Botez, R. (2017). Methodology of estimation of aerodynamic coefficients of the UAS-S4 ethical using Datcom and VLM procedure. In *AIAA Modeling and Simulation Technologies Conference*. AIAA. https://doi.org/10.2514/6.2017-3152

Kurdianto, Rahmat, M. Z., Islami, G. I., Rustamaji, Fakhri, M., Rahardiyanti, K., Sudiana, O., Arisandi, E. D., Purnomo, H., & Ibadi, M. (2023). Analysis of the effects of composite materials on the rocket nosecone on VSWR value of 900MHZ antenna frequency. In *2023 3rd International Conference on Innovative Research in Applied Science, Engineering and Technology (IRASET)* (pp. 1–5). IEEE. https://doi.org/10.1109/IRASET57153.2023.10152912

Logan, D. L., & Widera, G. E. O. (1989). Membrane theory for anisotropic laminated shells of revolution. *Journal of Pressure Vessel Technology*, *111*(2), 130–135. https://doi.org/10.1115/1.3265649

Loth, E., Tyler Daspit, J., Jeong, M., Nagata, T., & Nonomura, T. (2021). Supersonic and hypersonic drag coefficients for a sphere. *AIAA Journal*, *59*(8), 3261–3274. https://doi.org/10.2514/1.J060153

Lubecki, M., Stosiak, M., Skačkauskas, P., Karpenko, M., Deptuła, A., & Urbanowicz, K. (2022). Development of composite hydraulic actuators: A review. *Actuators*, *11*(12), Article 365. https://doi.org/10.3390/act11120365

Mathew, B. C., Bandyo, O., Tomar, A., Kumar, A., Ahuja, A., & Patil, K. (2021). A review on computational drag analysis of rocket nose cone. *Proceedings of the Workshop on Control and Embedded Systems (WCES 2021)*, *2875*(1), 95–105.

Purwoko, Vicarneltor, D. N., Purnomo, H., Najati, N., Rifa'i, M. J., Rizkyta, A. G., Setianto, M. H., Ibadi, M., Andiarti, R., Yunus, M., & Azhari, A. (2023, October). Assessment of composite radome impacts on the signal transmission of the 2.4 GHz frequency band. In *2023 IEEE International Conference on Aerospace Electronics and Remote Sensing Technology (ICARES)* (pp. 1–5). IEEE. https://doi.org/10.1109/ICARES60489.2023.10329894

Reddy, J. N. (2007). *Theory and analysis of elastic plates and shells* (2nd ed.). CRC Press. https://doi.org/10.1201/9780849384165

Sayyad, A. S., & Ghugal, Y. M. (2019). Static and free vibration analysis of laminated composite and sandwich spherical shells using a generalized higher-order shell theory. *Composite Structures*, *219*, 129–146. https://doi.org/10.1016/j.compstruct.2019.03.054

Shadmehri, F., Hoa, S. V., & Hojjati, M. (2012). Buckling of conical composite shells. *Composite Structures*, *94*(2), 787–792. https://doi.org/10.1016/j.compstruct.2011.09.016

Shi, Y., Cheng, Q., Alizadeh, A., Yan, H., Choubey, G., Fallah, K., & Shamsborhan, M. (2023). Influence of lateral single jets for thermal protection of reentry nose cone with multi-row disk spike at hypersonic flow: Computational study. *Scientific Reports*, *13*(1), 6549–6549. https://doi.org/10.1038/s41598-023-33739-2

Srivastava, L., Krishnanand, L., Kishore Nath, N., Hirwani, C., & Babu, M. (2022a). Online structural integrity monitoring of high-performance composite rocket motor casing. *Materials Today: Proceedings*, *56*, 1001–1009. https://doi.org/10.1016/j.matpr.2022.03.230

Srivastava, L., Krishnanand, L., Behera, S., & Kishore Nath, N. (2022b). Failure mode effect analysis for a better functional composite rocket motor casing. *Materials Today: Proceedings*, *62*, 4445–4454. https://doi.org/10.1016/j.matpr.2022.04.933

Tita, V., Caliri Júnior, M. F., & Massaroppi Junior, E. (2011). Theoretical models to predict the mechanical behavior of thick composite tubes. *Materials Research*, *15*(1), 70–80. https://doi.org/10.1590/S1516-14392011005000092

Tsushima, N., & Su, W. (2017). Concurrent active piezoelectric control and energy harvesting of highly flexible multifunctional wings. *Journal of Aircraft*, *54*(2), 724–736. https://doi.org/10.2514/1.C033846

Ugural, A. C. (2017). *Plates and shells: Theory and analysis* (4 ed.). CRC Press. https://doi.org/10.1201/9781315104621

Ukirde, K., & Rathod, S. (2023). Aerodynamic analysis of various nose cone geometries for rocket launch vehicle at different Mach regimes. *AIP Conference Proceedings*, *2855*(1). https://doi.org/10.1063/5.0179070

Ventsel, E., & Krauthammer, T. (2001). *Thin plates and shells: Theory, analysis and applications*. CRC Press. https://doi.org/10.1201/9780203908723

Zawawi, M. H., Saleha, A., Salwa, A., Hassan, N. H., Zahari, N. M., Ramli, M. Z., & Muda, Z. C. (2018). A review: Fundamentals of computational fluid dynamics (CFD). *AIP Conference Proceedings*, *2030*(1). https://doi.org/10.1063/1.5066893

Zingoni, A., & Enoma, N. (2020). On the strength and stability of elliptic toroidal domes. *Engineering Structures*, *207*, Article 110241. https://doi.org/10.1016/j.engstruct.2020.110241

Notations

Variables and functions

[A] – the extensional stiffness matrix, GPa;

[B] – the extensional-flexural coupling stiffness matrix, GPa;

$[B_0]$, $[B_l]$ – gradient of shape function containing the determinant of Jacobian matrix;

$[B_m]$ – gradient of shape function;

[C] – fourth order constitutive tensor, GPa;

[D] – the flexural stiffness matrix, GPa;

[N] – matrix of shape function;

$\{\varepsilon\}$ – nodal strain vector, m/m;

$\{\sigma\}$ – nodal stress vector, Pa;

$\{F\}$ – nodal force vector, N;

$\{T\}$ – surface traction vector, N;

$\{U\}$ – nodal displacement vector, m;

$\{X\}$ – body forces vector, N;

A_e – limit of integration for element surface integral;

c – cos θ;

E – Young's moduli of the steel, GPa;

E_1 – Young's moduli of the composite in directions 1, GPa;

E_2 – Young's moduli of the composite in directions 2, GPa;

F_D – the force acting at the front/top end of the shell structure of revolution, N;

$F_{D,n}$ – the aerodynamic drag force per unit segment, N;

F_n – the resultant force per each segment F_n perpendicular to segment Δx, N;

G_{12} – the shear modulus of the composite in the 1 and 2 planes direction, GPa;

G_{13} – the shear modulus of the composite in the 1 and 3 planes direction, GPa;

G_{23} – the shear modulus of the composite in the 2 and 3 planes direction, GPa;

L – the length of the nose cone, m;

M_{ns}, M_n – edge bending moment on a plate element, N.m;

M_x – bending stress resultant in global laminate x-direction, N/m;

M_{xy} – twist moment stress resultant in global xy-plane of laminate, N/m;

M_y – bending stress resultant in global laminate x-direction, N/m;

n – exponent value of the Power series nose cone design's formula;

N_ϕ – membrane stress resultant along the shell of revolution's meridian curve, N/m;

N_θ – membrane stress resultant along the shell of revolution's parallel curve, N/m;

N_x – normal stress resultant in global laminate x-direction, N/m;

N_{xy} – shear stress resultant in global xy-plane of laminate, N/m;

N_y – normal stress resultant in global laminate y-direction, N/m;

p_z – the axisymmetric pressure distribution on the shell structure, Pa;

q – distribution load on a plate element, N/m;

Q – the laminate stiffness matrix in global coordinates, GPa;

Q_l – the local laminate stiffness matrix, GPa;

R – the base radius of the nose cone, m;

r_0 – the radius of the circle on the parallel plane, m;

r_1 – radii of curvature in the meridian direction, m;

r_2 – radii of curvature in the parallel direction, m;

s – sin θ;

s_l – limit of integration for element line integral;

T – the transformation matrix;

T_n – transverse force acting on a plate element, N;

V_e – limit of integration for element volume integral;

$x = f(y)$ – contour function of the shell of revolution with respect to its axis, m;

y – radius of the parallel circle for each value of x, m;

z – distance between the neutral axis of the laminate cross-section to the i-th laminae, m;

φ – edge rotation angle of a plate element, rad;

θ – fibre orientation angle, deg;

ν – Poisson's ratio;

ρ – the density of steel, kg/m^3;

$\nu_{12} = \nu_{21}$ – In-plane Poisson's ratio;

Δx – small shell surface segment, m;

ε_{x0} – midplane normal strain in global laminate x-direction, m/m;

γ_{xy0} – midplane shear strain in global xy-plane of laminate, m/m;

ε_{y0} – midplane normal strain in global laminate y-direction, m/m.

Abbreviations

CAD – Computer-Aided Design;
CAE – Computer-Aided Engineering;
CFD – Computational Fluid Dynamics;
CLT – Classical Laminate Theory;
DATCOM – US Air Force Data Compendium;
FEM – Finite Element Method;
GEL – Global Element Length;
MPC – Multi-Point Constraint;
Quad – Quadrilateral;
RBE2 – Rigid Bar Element 2;
Tria – Triangular;
UAV – Unmanned Aerial Vehicle;
UD – Unidirectional.